The limits of narrow and wide-angle AVA inversions for high *Vp/Vs* ratios: an application to elastic seabed characterization

Aleardi Mattia, Tognarelli Andrea

University of Pisa, Earth Sciences Department

Corresponding author: Mattia Aleardi, email: mattia.aleardi@dst.unipi.it

Abstract

Since its introduction in the oil and gas industry, Amplitude Versus Angle (AVA) inversion has become a standard tool in deep hydrocarbon exploration. However, with the intensification of offshore construction activity, applications of this method have been extended to evaluate the elastic properties of seabed sediments and of the shallowest part of the subsurface. These regions are often characterized by undercompacted sediments with very low S-wave velocities (*Vs*) and high P-wave velocity to S-wave velocity (*Vp/Vs*) ratios. However, the importance of the *Vp/Vs* ratio is usually underrated in AVA inversion. In this study, we analyse the limits of the AVA method in cases of high *Vp/Vs* ratios and the benefits introduced by wide-angle reflections in constraining the results. A simplified seabed model that is characterized by a high *Vp/Vs* ratio is used to study the influence of the elastic and viscoelastic parameters on the P-wave reflection coefficients and to compute the error function of the AVA inversion. In addition, a synthetic AVA inversion is performed on this simplified model, which enables us to apply the sensitivity analysis tools to the inversion kernel. These theoretical analyses show that in the case of high *Vp/Vs* ratios, the *Vs* contrast at the reflecting interface plays a very minor role in determining the P-wave reflection coefficients and that the viscoelastic effects can be neglected when only pre-critical angles are considered in the inversion. In addition, wide-angle reflections are essential to reducing both the cross-talk between the inverted elastic parameters and the uncertainties in the

Vp and density estimations, but they are not sufficient to better constrain the *Vs* estimation. As an application to field data, we derive the elastic properties of the seabed interface by applying AVA inversion to a 2D seismic dataset from a well-site survey acquisition. The limited water depth, the maximum available source-to-receiver offset, and the high frequency content of the data allow two different ranges of incidence angles to be considered: 0-30 degrees and 0-60 degrees. The results of the field data inversion confirm the conclusions from the theoretical analysis.

Keywords

Amplitude versus angle inversion, high Vp/Vs ratios, seabed characterization

1. Introduction

The increase in offshore exploration and intensive construction activity has required reliable characterizations of the properties of the seabed and shallow sediments to minimize the risk of harm to personnel and equipment during drilling operations, to prevent accidents to the natural environment and to identify safe zones to install structures such as platforms, oil rigs, and pipelines. The results of seismic data inversion are often used to determine the elastic properties of the shallowest part of the subsurface and to identify possible shallow hazards. Once the elastic properties are derived, they can be converted into the geotechnical properties that are needed for engineering purposes.

Amplitude Versus Angle (AVA) inversion can be used to derive the elastic properties of the subsurface. Since the 1980s, this method has been used extensively worldwide for lithological and fluid prediction in hydrocarbon exploration (e.g., Ostrander, 1984; Rutherford and Williams, 1989; Mazzotti, 1990; Grion et al., 1998, Mazzotti and Zamboni, 2003; Wang, 2003; Downton, 2005; Grana and Della Rossa, 2010). Over the last several decades, AVA inversion has also been extended to shallow hazard assessment and well site analysis (Theilen and Pecher, 1990; Ayres and Theilen, 1999; Riedel and Theilen, 2001; Riedel et al., 2003). In these contexts, sediments with very low S-wave velocities and high P-wave velocity to S-wave velocity (*Vp/Vs*) ratios are often encountered.

Despite its many successful applications, AVA inversion suffers from many limitations and physical ambiguities, which are clearly discussed in Drufuca and Mazzotti (1995). Moreover, as discussed in Aleardi (2015), these physical ambiguities increase as the *Vp/Vs* ratio increases. To the best of our knowledge, this particular limitation of AVA inversion has not received much attention and has not yet been extensively discussed, especially in the case of field data. Many authors have pointed out that the physical ambiguities of AVA inversion can be greatly reduced by exploiting amplitude information that is extracted near and beyond the critical angle (e.g., Avseth et al., 2005). In the context of wide-angle AVA inversion, post-critical reflections have been demonstrated to be crucial for better constraining estimates of the viscoelastic properties (Riedel et al., 2003) and anisotropy parameters (Skopintseva and Alkhalifah, 2013), whereas Zhu and McMechan (2012) noted that even the Phase Versus Angle (PVA) information can be used to reduce the ambiguities of the results. In addition, many authors have pointed out that in the case of wide-angle AVA inversions, the Zoeppritz equations that consider a plane wave front become inadequate (Ursenbach et al., 2007; Skopintseva et al., 2011; Zhu and McMechan, 2012; Alulaiw and Gurevich, 2013). In practice, real seismic surveys use localized sources that produce spherical waves rather than plane waves. In the far-field, the AVA response for a spherical wave reflected from a planar interface can be approximated well by a plane wave response. This approximation breaks down in the vicinity of the critical angle, where spherical wave effects become important. However, the spherical wave reflection coefficients approach the plane wave reflection coefficients as the frequency of the propagating wave increases.

Over the last few decades, the introduction of long recording cables/streamers and new acquisition methods has enabled the recording of long-offset reflections, which has increased the interest in wide-angle AVA inversion. However, the benefits of wide-angle reflections in AVA inversion have been discussed and demonstrated primarily based on synthetic data (Skopintseva et al., 2011; Zhu and McMechan, 2012; Alulaiw and Gurevich, 2013), whereas applications of wide-angle AVA inversion to field data are extremely rare, and their results are often controversial (Avseth et al., 2005). The applicability of wide-angle AVA inversion is mainly limited by two factors. First, the AVA method only considers primary reflections and cannot easily handle interfering events, which become significant near and beyond the critical angle. Second, the industry has little experience in processing and interpreting long-offset data because these data have traditionally been muted during seismic processing. In PVA inversion, the phase of the reflected signal is affected much more by residual noise contamination than the amplitude information. Therefore, applications of wide-angle PVA inversion to field data are even rarer than AVA inversions. In conclusion, although this research field is currently undergoing further and promising developments, the applicability of AVA or PVA inversions to long-offset seismic data is strongly case-dependent. For example, as shown in Aleardi (2014), the applicability of these wide-angle inversion methods is strongly influenced by the frequency content of the data because the interference effects that characterize wide-angle reflections decrease as the frequency content (and thus the resolution) of the data increases.

In this paper, we analyse the limits of AVA inversion in the case of high *Vp/Vs* ratios and demonstrate the benefits of wide-angle reflections in constraining the results. After a brief review of the AVA method, we describe the inversion procedure that we apply. Then, considering a theoretical seabed model with a high *Vp/Vs* ratio, we study the effect of the elastic and viscoelastic properties on the AVA and PVA responses and quantify the effect of wide-angle reflections in constraining the inversion. To this aim, we compute the 2D and 1D error functions associated with the AVA inversion and perform a sensitivity analysis on the inversion kernel. Simple synthetic inversions are discussed before introducing the field data processing and inversion.

2. Theoretical background of AVA inversion

For the idealized case of a plane wave incident on a horizontal interface that separates two semi-infinite elastic and homogeneous half-spaces, Zoeppritz (1919) derived the expressions for the reflection coefficients as a function of the angle of incidence. Based on the Zoeppritz equations, Aki and Richard (1980) provided an approximation for the P-P wave reflection coefficients parameterized in terms of elastic contrasts at the reflecting interface. This approximation is valid for small physical contrasts at the reflecting interface and small incidence angles (generally less than 30-35 degrees):

$$R_{pp}(\theta)=\frac{1}{2\cos^2\theta}\frac{\Delta\alpha}{\bar{\alpha}}-4\gamma^2\sin^2\theta\frac{\Delta\beta}{\bar{\beta}}-\frac{1}{2}(4\gamma^2\sin^2\theta-1)\frac{\Delta\rho}{\bar{\rho}} \qquad (1)$$

where $\overline{\alpha}$, $\overline{\beta}$ and $\overline{\rho}$ are the average P-wave velocity, S-wave velocity and density, respectively, over the reflecting interface, $\Delta\alpha$, $\Delta\beta$ and $\Delta\rho$ are the corresponding contrasts, R_{PP} is the P-wave reflection coefficient, θ is the average of the incident and transmitted P-wave angles, and γ is inversely correlated with the background *Vp/Vs* ratio:

$$\gamma = \frac{\beta_1 + \beta_2}{\alpha_1 + \alpha_2} \qquad (2)$$

where the subscripts 1 and 2 refer to the overlying and underlying layers, respectively.

In most contexts, linear approximations are accurate, simpler and more practical than the Zoeppritz equations; thus, they form the basis of AVA inversion. However, simple observations of the Aki and Richards approximation (equation 1) or any other type of linear simplification of the Zoeppritz equations clearly show that their parameterization is not suitable for a fluid-solid interface. In fact, these parameterizations do not allow the extraction of the S-wave velocity contrast at the fluid-solid reflecting interface, where for each *Vs* value of the solid medium, the $\Delta\beta/2\overline{\beta}$ term (the so-called S-wave reflectivity contrast) is equal to one. Therefore, for a complete estimation of the seabed properties, we need to use a different equation with a different parameterization that allows us to evaluate the S-wave velocity contrast at the seabed interface. We use the exact Zoeppritz equations that are locally linearized with the Gauss-Newton iterative method. Aleardi (2015) demonstrated that the stability, predictive capability, and physical meaning of the linear AVA inversion change with the background *Vp*/*Vs* ratio. Thus, to stabilize the inversion process, we use the Tikhonov regularization, in which the regularization term is estimated by means of the so-called trade-off curve. In the inversion, the Jacobian matrix, which is needed to update the current estimated model, is computed by means of a finite difference approach. After the inversion, the error propagation from the data to the model space is performed by applying a Monte Carlo approach and by assuming Gaussian distributed errors and Gaussian distributed elastic properties. More details about the Gauss-Newton method, Tikhonov regularization and the Monte Carlo approach to error estimation are discussed in the following section. We refer the reader to Aster et al. (2005) for full mathematical details.

3. AVA inversion with the Gauss-Newton method

The goal of any seismic inversion is to find a set of subsurface parameters by minimizing the data misfit Δd between the observed data d_{obs} and the predicted data d_{pre}. This misfit can be measured by the following error function:

$$E(m) = \frac{1}{2} \Delta d^T \Delta d \qquad (3)$$

where the data residual vector is $\Delta d = d_{obs} - d_{pre}$, and the superscript T denotes the matrix transpose operator. Local minimization of the misfit function in the vicinity of the model m_n at iteration n gives the Newton descent direction p_n as:

$$p_n = -[H(m_n)]^{-1} \nabla_m E(m_n) \qquad (4)$$

where $\nabla_m E$ and $H(m)$ are the first and second derivatives, respectively, of the misfit function with respect to the model parameters. They are also referred to as the gradient and the Hessian of the misfit function, respectively:

$$\nabla_m E = \frac{\partial E}{\partial m} = -\left(\frac{\partial d_{pre}}{\partial m}\right)^T \Delta d = -J^T \Delta d \qquad (5)$$

$$H(m) = \frac{\partial^2 E}{\partial^2 m} = J^T J + \left(\frac{\partial J}{\partial m}\right)^T \Delta d \qquad (6)$$

where J is the sensitivity kernel, which is also called the Jacobian matrix. The minimum of the misfit function in the vicinity of the initial model m_0 is reached when the first derivative of the misfit function vanishes. This gives the perturbation model vector at iteration n:

$$\Delta m_n = -\left(\frac{\partial^2 E(m_n)}{\partial^2 m}\right)^{-1} \frac{\partial E(m_n)}{\partial m} \qquad (7)$$

Under the Born approximation, the data residual is very small, and the relationship between the seismic data and the model parameters is weakly non-linear; thus, the second term in the Hessian operator can be neglected, and the Hessian operator can be reduced to the approximated Hessian H_a:

$$H_a(m) = J^T J \qquad (8)$$

The method that only uses H_a is referred to as the Gauss-Newton method. Alternatively, the inverse of the Hessian can be replaced by a scalar, the so-called step length, which leads to the steepest-descent method. Therefore, the general formula that expresses the model update for the Gauss-Newton method in matrix notation is:

$$\Delta m = \left(J^T J\right)^{-1} J^T \Delta d \qquad (9)$$

Experimental measurements are always affected by noise, which is often conveniently assumed to be Gaussian distributed with a zero mean. To account for this noise in the inversion, equation 9 can be re-written as:

$$\Delta m = \left(J^T C_d^{-1} J\right)^{-1} J^T C_d^{-1} \Delta d \qquad (10)$$

where C_d is the data covariance matrix associated with the noise distribution.

The computation of the inverse of the approximated Hessian is often non-stable. In particular, in the context of AVA inversion, the stability of the problem decreases as the *Vp/Vs* ratio increases (Aleardi, 2015). To stabilize the inversion, we apply the well-known Tikhonov regularization, with which the inverse of the approximated Hessian can be computed as follows:

$$H_a^{-1} = (J^T J + \lambda I)^{-1} \qquad (11)$$

where I is the identity matrix, and λ is the regularization parameter. To determine the damped parameter λ, we use the so-called trade-off curve (also called the *L*-curve; see Aster et al., 2005), and we select the λ value that minimizes both the norms in the data and model space.

From these considerations, the final equation that we use to update the current model is:

$$\Delta m = \left(J^T C_d^{-1} J + \lambda I\right)^{-1} J^T C_d^{-1} \Delta d \qquad (12)$$

We apply a finite difference approach to compute the Jacobian matrix. With this method, the partial derivative of the data predicted at the *n*-th iteration with respect to the *j*-th model parameter is computed as follows:

$$\frac{\partial d^n_{pre}}{\partial m_j} \approx \frac{G\left(m_n + h_j\right) - G\left(m_n\right)}{h_j} \qquad (13)$$

where h_j indicates an arbitrary increment of the *j*-th model parameter, and G is the forward modelling operator that relates the model to the data (in our case, the exact Zoeppritz equations).

After the inversion, the error propagation from the data to the model space is performed by applying a Monte Carlo approach and assuming that the posterior uncertainties follow a Gaussian distribution. This method is often applied to non-linear problems for which there is no simple way to propagate the uncertainties in the data to uncertainties in the estimated model parameters. We apply this method instead of the classical Bayesian formulation because no a-priori information is available in the investigated area to build a reliable prior model in terms of an a-priori model covariance matrix and a-priori expectations. In Monte Carlo error propagation techniques, a collection of noisy data vectors is simulated, and the statistics of the corresponding models are then examined. We can obtain an approximate posterior covariance matrix by first forward-propagating the solution that was obtained from the previous inversion (m_{pre}) into an assumed noise-free baseline data vector (d_b):

$$d_b = G(m_{pre}) \qquad (14)$$

Starting from this noise-free data vector, the inversion can be repeated Q times considering a set of Q independent data realizations, where the *i*-th data realization is obtained by adding a noise vector to the data d_b (we assume a Gaussian distributed noise with a zero mean):

$$d_b^i = d_b + \eta_i \qquad (15)$$

where η_i is the *i*-th noise vector realization. From these *Q* inversions, a suite of *Q* solutions is obtained. Let *A* be a *Q*×*M* matrix (where *M* indicates the number of unknown parameters) in which the *i*-th row contains the difference between the *i*-th model extracted from the *Q* inversion results and the final model estimated by the AVA inversion (m_{pre}). An empirical estimate of the model covariance matrix (C_m) can then be computed as follows:

$$C_m = \frac{A^T A}{Q} \qquad (16)$$

The P-wave velocity, S-wave velocity and density are always correlated and, as discussed in Downton (2005), if some a-priori information about this correlation can be derived from available additional data (i.e., well log or core data) or from empirical relations, its inclusion in the inversion kernel can help to stabilize the inversion and speed up the convergence. Unfortunately, in our specific case, no well log or core data are available for the investigated area, and the available empirical relations (such as those of Hamilton, 1976) are too generic to be safely used without the risk to bias the solution.

4. Studying the influence of seabed characteristics on P-wave reflection coefficients

In this section, we quantify the influence of the seabed's physical properties on the AVA and PVA responses. We consider a theoretical seabed model in which the *Vp, Vs* and density of the seabed sediments are equal to 1700 m/s, 200 m/s and 1.2 g/cm^3, respectively, and the *Vp* and density of the water are equal to 1500 m/s and 1 g/cm^3, respectively. Note that the *Vp/Vs* ratio for the seabed sediments is equal to 8.5, which is a very high value that is common in strongly undercompacted sediments. However, shallow marine sediments are more realistically described as absorbing materials than as purely elastic. Therefore, we also analyse the differences between a perfectly elastic seabed and a more realistic viscoelastic material.

In the following modelling exercises, we ignore the influence of a spherical wave front on the P-wave reflection coefficients and assume a plane wave incident on a horizontal interface that separates two semi-infinite homogeneous half-spaces. This allows us to use the simple Zoeppritz equations for the forward modelling. The following examples are intended to provide a practical demonstration of the difficulty of estimating the S-wave velocity of seabed sediments that are characterized by low *Vs* values and high *Vp/Vs* ratios.

4.1 AVA modeling: Elastic materials

We first model the influence of different sediment properties on the P-wave reflection coefficients as a function of the angle of incidence for an elastic sediment model (i.e., considering only the P- and S-wave velocities and the bulk density). In this exercise, we consider the seabed model that was previously described, and we vary the elastic properties of the seabed around their true value by ± 10%. The water properties are kept fixed at their true values.

In general, the P-wave reflection coefficients for an elastic model are dominated by the critical angle, at which no P-wave energy is transmitted into the sediment. Increasing the P-wave velocity of the sediment decreases the critical angle and increases the overall reflection coefficients. There are clear differences between lower and higher velocities in the wide-angle domain above 40 degrees (Figure 1a). Even though the seabed interface in the model is characterized by a relatively high S-wave velocity contrast, it does not significantly influence the AVA trend (Figure 1b). It is apparent that if lower S-wave velocities for the seabed sediments were considered (from 10 m/s to 100 m/s), the reflection coefficients shown in Figure 1b would be even more similar. In contrast to *Vp*, the influence of the sediment density is enhanced in the low-angle domain below 40-50 degrees (Figure 1c). A direct consequence of the Zoeppritz equations is that changes in the density and *Vs* affect the reflection coefficient but do not change the critical angle of the reflected signal. Moreover, over the ranges of values that we are considering, *Vs* and density exert less of an influence on the phase of the reflected signal than *Vp* (Amundsen and Reitan, 1995). Therefore, the phase versus angle trend is only analysed as *Vp* varies (Figure 1d); this analysis reveals that for an elastic medium, a phase shift occurs only for post-critical angles. This simple example demonstrates the limits of the AVA method in evaluating the low S-wave velocities that often characterize shallow marine environments. In these geological contexts, the estimation of the S-wave velocity is a hopelessly ill-conditioned problem even if wide-angle reflections are considered. Conversely, we expect that wide-angle reflections may be crucial to better constrain density and, particularly, *Vp* estimates.

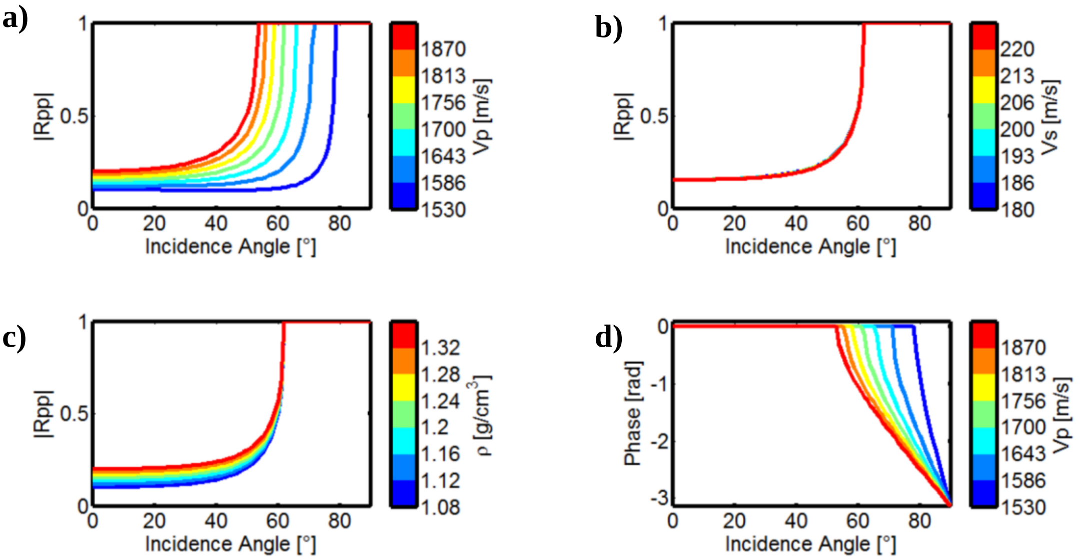

Figure 1: Influence of the elastic seabed properties on the P-wave reflection coefficients for a perfectly elastic seabed model (a, b and c). The Vp, Vs and density of the reference elastic seabed model are varied in a), b) and c), respectively. Influence of the P-wave velocity of the seabed on the phase signal (d). In all cases the water properties are kept fixed at their true values.

4.2 AVA modeling: Viscoelastic materials

The mathematical details of viscoelastic AVA modelling are given in Riedel and Theilen (2001). In this paper, we only remark that the attenuated wave has a complex and frequency-dependent velocity and that the viscoelastic reflection coefficients as a function of the angle of incidence can be calculated using the classical Zoeppritz equations, in which the velocities are replaced by their complex equivalents.

We model the viscoelastic reflection coefficients as a function of the angle of incidence using the same parameter variations that were previously considered in the elastic model but with a quality factor *Q*=10 for both the P-wave and S-wave velocities. In addition, to avoid the effects of the frequency dependence of the phase velocity, the reflection coefficients are modelled for a propagating frequency of 50 Hz. The general difference between the elastic and viscoelastic P-wave reflection coefficients is the absence of a critical angle effect in the viscoelastic case (Jensen et al., 2011). As expected, both the P-wave velocity and density have a strong influence on the reflection coefficients. Significant changes are observed in the wide-angle domain as the P-wave velocity varies (Figure 2a) and in the low-angle domain as the density varies (Figure 2c). Again, the S-wave velocity has a negligible effect on the P-wave reflection coefficients (Figure 2b). In contrast to the elastic case, in viscoelastic modelling, the phase shift also occurs for pre-critical angles (Figure 2d).

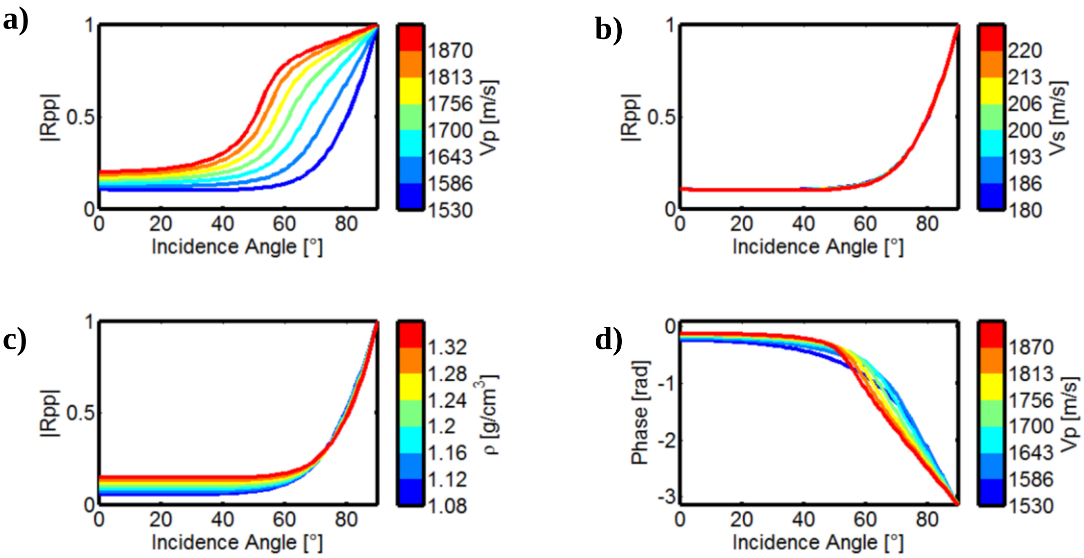

Figure 2: Influence of the elastic seabed properties on the P-wave reflection coefficients (a, b and c) for a viscoelastic seabed sediment with Qp and Qs equal to 10. Only the Vp, Vs and density of the reference viscoelastic seabed model are varied in a), b) and c), respectively. Influence of the P-wave velocity of the seabed on the phase signal (d). In all cases the water properties are kept fixed at their true values.

Figure 3 illustrates the influence of the viscoelastic parameters (the quality factors for the P- and S-waves, which are indicated by Q_p and Q_s, respectively) on the P-wave reflection coefficients. We consider the viscoelastic seabed model that was considered previously, but in this case, only the quality factors of the seabed sediments are varied. The influence of Q_p on the reflection coefficients is enhanced in the wide-angle domain because it can only be seen above the critical angle, which is defined by an equivalent elastic model. Increases in Q_p move the P-wave reflection coefficients towards a more elastic-shaped function (Figure 3a). In the case of high Q_p values (i.e., Q_p=100), there is no significant difference between the elastic and viscoelastic models. In particular, the effect of Q_p on the P-wave reflection coefficients is much more pronounced than the effect of Q_s (Figure 3b). Therefore, this modelling study illustrates that estimating the Q factors from an AVA inversion is usually a non-unique problem, particularly for the Q_s parameter, even if a wide-angle domain is considered (Riedel et al., 2003).

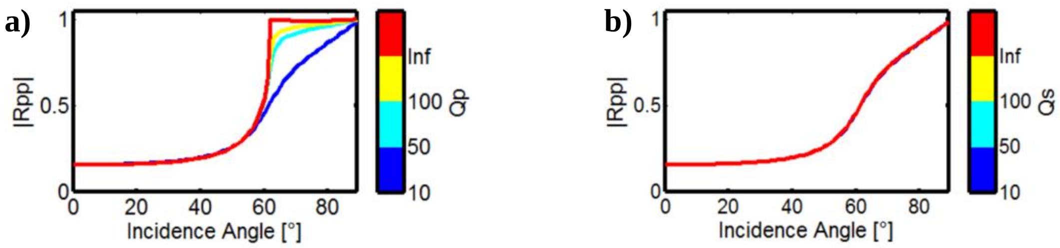

Figure 3: Influence of the P- and S-wave quality factors of the seabed sediments on the P-wave reflection coefficients. a) Influence of Qp for a fixed Qs value of 10. b) Influence of Qs for a fixed Qp value of 10.

5. Studying the error function

As shown previously, the forward problem given by the Zoeppritz equations appears to be highly insensitive to low S-wave velocities. One possibility for mapping the insensitivity is to observe the error function of the AVA inversion that is computed by considering the reference elastic seabed model and by varying the P- and S-wave velocities and densities. This exercise allows us to quantify the benefits, both in increased resolution and decreased ambiguity, that are produced in the error function if the amplitudes associated with wide-angle reflections are considered in the inversion. In the following discussion, we consider both 1D and 2D representations of the error function, which are computed by varying the sediment properties one or two at a time, respectively. For simplicity, we consider a fully elastic model and keep the water properties fixed at their true values. The error function that we consider is given by the L_2 norm between the observed and predicted R_{pp} responses:

$$error = \sum_{i=1}^{N} \left(R_{pp_i}^{\;pre} - R_{pp_i}^{\;obs} \right)^2 \qquad (17)$$

where N is the total number of reflection coefficients considered, and the superscripts *pre* and *obs* refer to the predicted and observed P-wave reflection coefficients, respectively. The computation is performed for two different angle ranges; from 0 to 30 degrees and from 0 to 60 degrees.

5.1 1D error functions

The investigation of the 1D error function shows that for incidence angles from 0 to 30 degrees, the reflection coefficient is primarily influenced by the P-wave velocity and density (Figure 4a, Figure 4b and Figure 4c). In fact, if only *Vp* and the density are varied, the error function shows a well-defined single minimum. In particular, the changes in the error function that are related to variations in *Vp* and density are more than two orders of magnitude greater than those produced by *Vs* variations. This result provides another clear demonstration of the difficulties related to *Vs* estimation for low *Vs* values. For a wider range of incidence angles from 0 to 60 degrees (Figure 4d, Figure 4e and Figure 4f), the values of the error function increase for each parameter with respect to the previous case. This trend clearly indicates that increasing the range of angles used in the inversion increases the expected resolution for each elastic parameter. In particular, the reflection coefficient shows its maximum sensitivity to variations in *Vp* due to the effect of the critical angle, which is only influenced by the P-wave velocity contrast at the reflecting interface. However, the *Vs* parameter exhibits a minor influence in determining the amplitude response compared with the other two elastic parameters in this example. In particular, the error function values that are associated with S-wave velocity variations remain close to zero for values less than 200 m/s. Conversely, the influence of this parameter on the R_{pp} response increases for higher *Vs* values. This behaviour demonstrates that in the case of very low S-wave velocities, the *Vs* parameter has a weak influence on the amplitude response of the reflecting interface, and its estimation will be a hopelessly ill-conditioned problem even if wide-angle reflections are considered. These results again highlight the difficulties related to a reliable *Vs* estimation for seabed sediments with a very low S-wave velocity. The influence of *Vs* in determining the P-wave reflection coefficients is sufficiently high to ensure a reliable estimation of this parameter only when sufficiently high values of this parameter are reached. In contrast, wide-angle reflections are crucial for better constraining the density and particularly the *Vp* estimation.

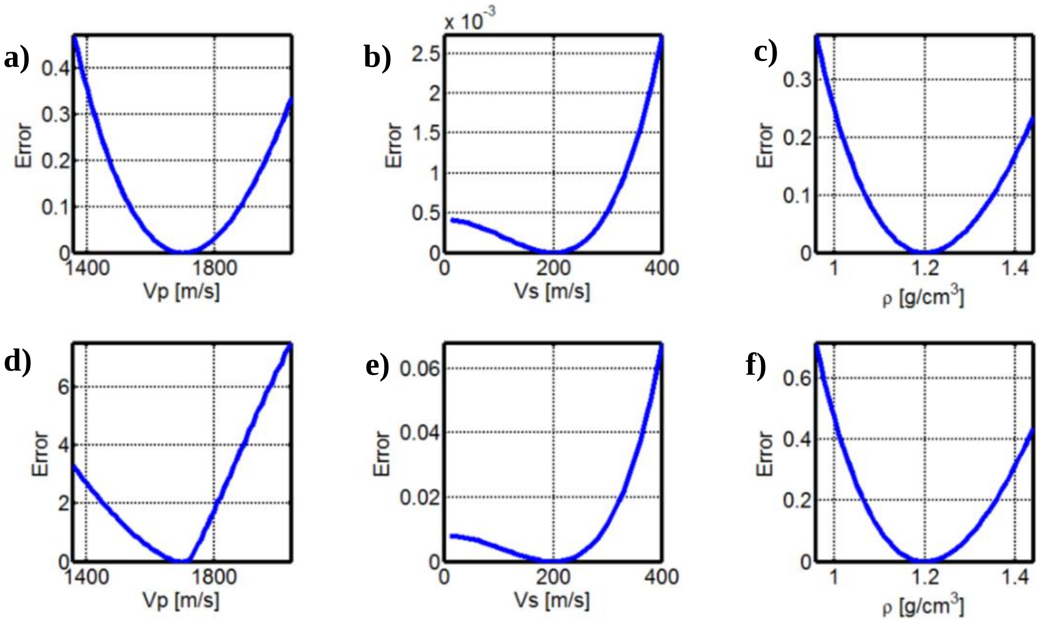

Figure 4: a), b) and c) 1D error functions obtained by varying the seabed properties one by one and considering a range of angles up to 30 degrees. d), e) and f) 1D error functions obtained by varying one by the seabed properties and considering a range of angles up to 60 degrees.

5.2 2D error functions

By varying the elastic properties of the seabed two at a time, we obtain the so-called 2D error function. As in the 1D example, we consider two different ranges of incidence angles; from 0 to 30 degrees and from 0 to 60 degrees. All of the figures in this section use the same colour scale to allow for a better comparison of their differences. Let us consider the first case, where only the narrow-angle information is used to compute the error function (Figure 5a). An elongated valley of minima that is roughly parallel to the *Vs* axis confirms the difficulty of estimating the seabed S-wave velocity. This figure also shows the fairly good resolution of the density parameter. Moreover, the orientation of this valley indicates the positive correlation between the density and *Vs*. Note that this valley moves toward lower density values as *Vp* increases, which indicates the negative correlation between *Vp* and density in determining the P-wave reflection coefficients. If we increase the range of angles up to 60 degrees, the resolution increases for the density and especially for *Vp*, whereas *Vs* remains poorly resolvable even in this case.

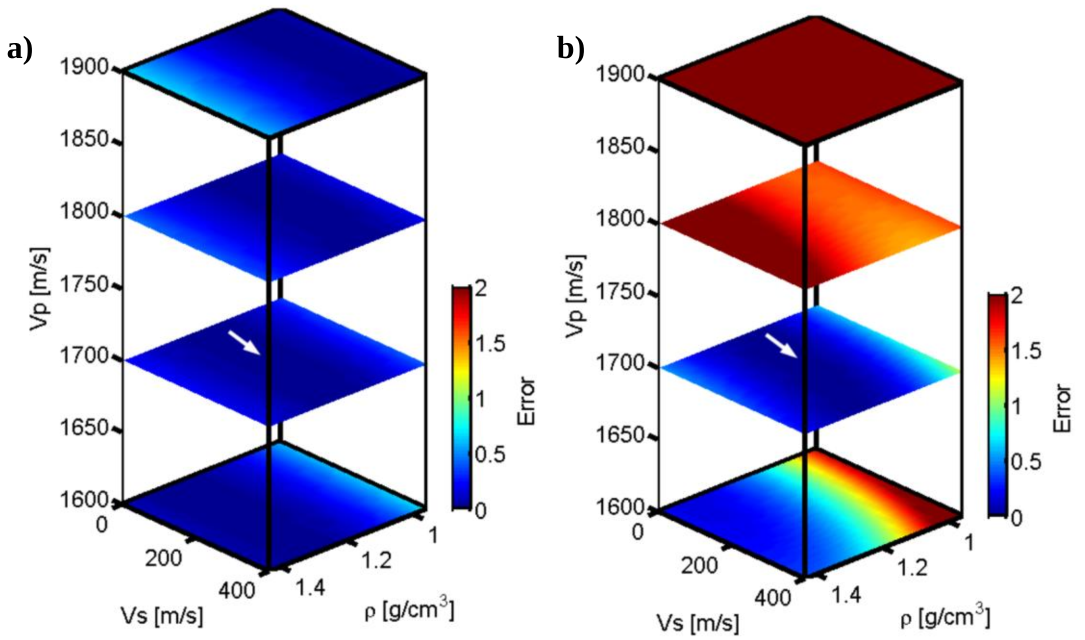

Figure 5: a) 2D error functions computed for four different Vp values as the density and Vs of the seabed are varied. In this case, a range of angles from 0 to 30 degrees is considered. b) 2D error functions computed for four different Vp values as the density and Vs of the seabed are

varied. In this case, a range of angles from 0 to 60 degrees is employed. In a) and b), the white arrows indicate the true property values.

6. Sensitivity analysis in the case of high *Vp/Vs* ratios

To further investigate the difference between the narrow- and wide-angle inversions and the limits of AVA inversion in the case of high *Vp/Vs* ratios, we can use the SVD decomposition (Aster et al., 2005) of the Jacobian matrix. The SVD decomposition of a generic matrix *G* can be expressed as:

$$G = USV^T \qquad (18)$$

where *S* is a diagonal matrix of singular values, *V* is the matrix of eigenvectors in the model space, and *U* contains the eigenvectors in the data space. The energy of each component is given by the corresponding eigenvalue. If the orders of magnitude of the eigenvalues are significantly different, a high signal-to-noise ratio is needed to estimate the signal in the low-energy directions. The SVD decomposition is essential in sensitivity analysis because it permits a better understanding of the physical meaning of the Jacobian matrix to be obtained. In fact, this decomposition allows the reflectivity R_{pp} to be divided into three orthogonal components in both the data space and the model space. The eigenvectors *V* are a basis in the model space. The eigenvalues *S* represent the reflected energy due to medium perturbations along the eigenvectors in the model space. The amplitude versus angle effects of the reflections are described by the eigenvectors in the data space (*U*), which are three orthogonal functions (De Nicolao et al., 1993).

In the case of a linearized iterative inversion algorithm, the relation between the model update and the data misfit can be generically expressed as follows:

$$\Delta m = J^{-g} \Delta d \qquad (19)$$

where Δm is the model update, Δd is the L_2 norm between the predicted data and the observed data, and J^{-g} is the so-called generalized inverse (Aster et al, 2005), which, in the case of the standard Gauss-Newton method, can be written as (also see equation 9):

$$J^{-g} = (J^T J)^{-1} J^T \qquad (20)$$

From the generalized inverse at the convergence point, the model resolution matrix can be derived as follows:

$$R = J^{-g} J \qquad (21)$$

where R is the model resolution matrix that expresses how the true model parameters are resolved in the inversion. Obviously, the farther the resolution matrix is from the identity matrix, the worse the resolution is (Tarantola, 2005).

Aleardi (2015) performed this sensitivity analysis for the case of linear AVA inversions while varying the *Vp/Vs* ratio. In this paper, the linearized approach that we apply allows us to extend this analysis over a wide range of incidence angles (between 0 and 60 degrees). The Jacobian matrix used in the following sensitivity analysis is derived from the inversion of the simple elastic seabed model that was introduced in section 4. In this inversion, the water properties are kept fixed, and only the seabed's elastic characteristics are considered as unknowns. The final results of the synthetic inversion will be described in section 7.

We analyse the variations in the singular values of the Jacobian matrix as the maximum incidence angle increases. By observing the singular values of the Jacobian matrix (Figure 6a), we observe that the first singular value contains almost all of the signal energy; the second singular value is negligible for small incidence angles and, although it increases at higher angles, is always 15-20 *dB* below the first. The amplitude of the third singular value is negligible for a range of angles between 0 and 40 degrees. In these cases, this singular value will be covered by noise and should be eliminated to stabilize the inversion. The amplitude of the third singular value becomes significant beyond 40 degrees, and in these cases, this singular value should be used in the inversion process. To better understand this figure, we can theoretically assume that the second or third singular values (and the associated eigenvectors) should be eliminated from the inversions if their amplitudes are -40 dB below the amplitude of the first singular value (Aleardi, 2015). This assumption demonstrates that for a limited range of angles between 0 and 15 degrees, only one linear combination of parameters (the combination that corresponds to the first eigenvector) can be reliably estimated. The estimation of two independent combinations (the first and second eigenvectors) requires a maximum incidence angle greater than 15-20 degrees. Obviously, these cases are characterized by a poorer signal-to-noise ratio in the direction of the second singular value. The estimation of three independent combinations of parameters is clearly an ill-conditioned problem in the case of a maximum incidence angle of less than 40-45 degrees. However, if we extend the range of angles to 60 degrees, the third singular value can also be used in the inversion, and three independent combinations of parameters can be estimated.

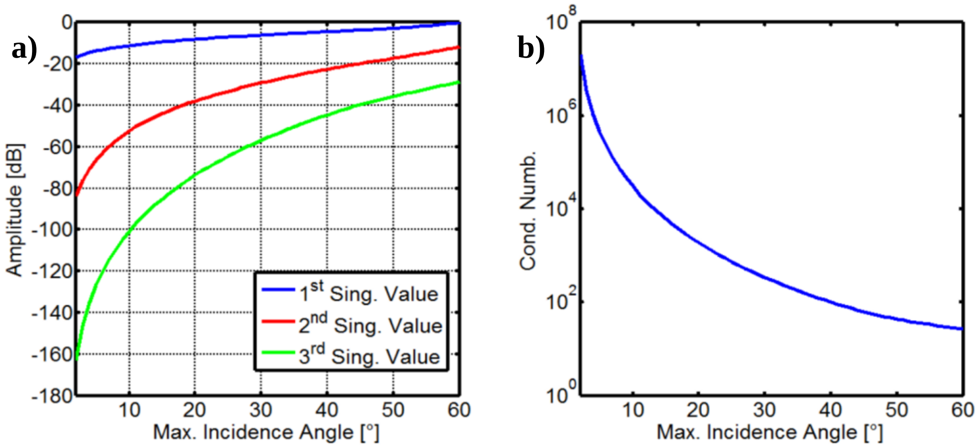

Figure 6: a) Singular values of the Jacobian matrix as the maximum incidence angle increases. b) Condition number of the Jacobian matrix as the maximum incidence angle considered in the inversion increases.

We now compute the condition number of the Jacobian matrix by varying the maximum incidence angle that is considered in the inversion. The condition number is the ratio between the highest and smallest singular values of a matrix, and high condition numbers are usually associated with ill-conditioned inverse problems. Figure 6b demonstrates that increasing the range of angles considered in the inversion decreases the condition number of the Jacobian matrix and tends to stabilize the inversion process. This clearly influences the regularization term that is inserted in the Tikhonov regularization (see equation 11), and the amplitude of this term should decrease as the maximum angle considered in the AVA inversion increases.

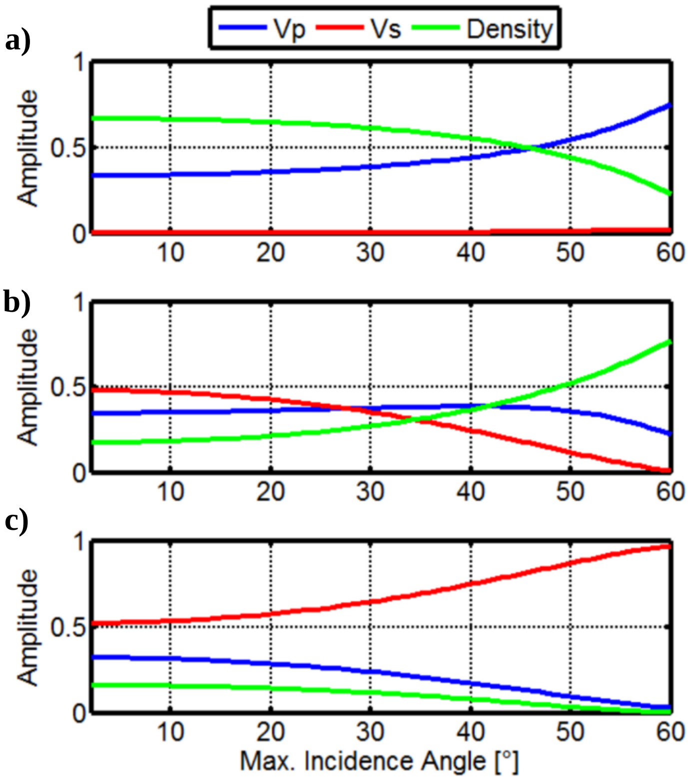

Figure 7: Eigenvectors in the model space versus the maximum incidence angle for a high Vp/Vs ratio. The components of the first, second and third eigenvectors are represented in a), b) and c), respectively.

Figures 7a, 7b and 7c represent the eigenvectors in the model space (*V*) associated with the first, second and third singular values of the Jacobian matrix, respectively, as the maximum incidence angle increases. In the first eigenvector, the *Vp* and density components are very similar for low angles. Therefore, this vector primarily points in the direction of the P-impedance perturbations. This result is obvious; the normal incidence reflection coefficient only depends on the acoustic impedance contrast. For high incidence angles, as the critical angle is approached, the density term decreases, while the *Vp* component strongly increases. This fact can be explained by considering that only the *Vp* parameter determines the critical angle of the R_{pp} reflection coefficients. The influence of *Vs* on the first eigenvector is null over the entire range of angles considered. The physical meanings of the second and third eigenvectors for low incidence angles are more difficult to interpret because they depend on combinations of different perturbations. However, for high incidence angles (beyond 40 degrees), it is clear that the second and third eigenvectors point toward the density and *Vs* parameters, respectively. In particular, we confirmed that the third eigenvector can be used in the inversion only if a very wide range of angles is considered. In fact, in a standard narrow-angle AVA inversion, the third singular value and the associated eigenvector (that contain information about the *Vs* parameter) are covered by noise and must be eliminated to stabilize the inversion. This makes a reliable estimation of the *Vs* value impossible. As shown in Figure 6, a wide range of angles makes it possible to use the third singular value (and the associated eigenvector) in the inversion, from which the *Vs* parameter can be estimated. However, it is important to note that *Vs* has a significant influence on only the third eigenvector; therefore, the *Vs* estimation will be much less accurate than the *Vp* and density estimations. A wide range of angles is particularly useful for decreasing the cross-talk between *Vp* and the density and to ensure independent estimations of these two parameters. In particular, only the P-impedance can be reliably estimated from the first eigenvector if a narrow range of angles is used. If we consider a maximum incidence angle range of up to 50-60 degrees, the first eigenvector points toward the *Vp* parameter, and the second points toward the density parameter. Thus, a wide range of angles makes it possible to independently estimate *Vp* and density from the first and the second eigenvectors, respectively.

Finally, we compare the model resolution matrices that are computed by considering angle ranges of 0-30 and 0-60 degrees (Figure 8a and 8b, respectively). From the main diagonal of the matrix in Figure 8a, we note that a narrow-angle inversion results in satisfactory resolutions for *Vp* and density and in a very low resolution for *Vs*. The off-diagonal terms demonstrate that *Vp* and density strongly influence each other. Figure 8b shows that increasing the range of angles up to 60 degrees significantly increases the expected resolutions for *Vp* and density, whereas only a minor improvement of the *Vs* resolution is produced. Figure 8b also shows a significant decrease of the off-diagonal terms compared to Figure 8a; this proves that a wide range of angles allows independent estimations of *Vp*, *Vs* and density. See Appendix A for an example of a sensitivity analysis in the case of a *Vp/Vs* ratio equal to two.

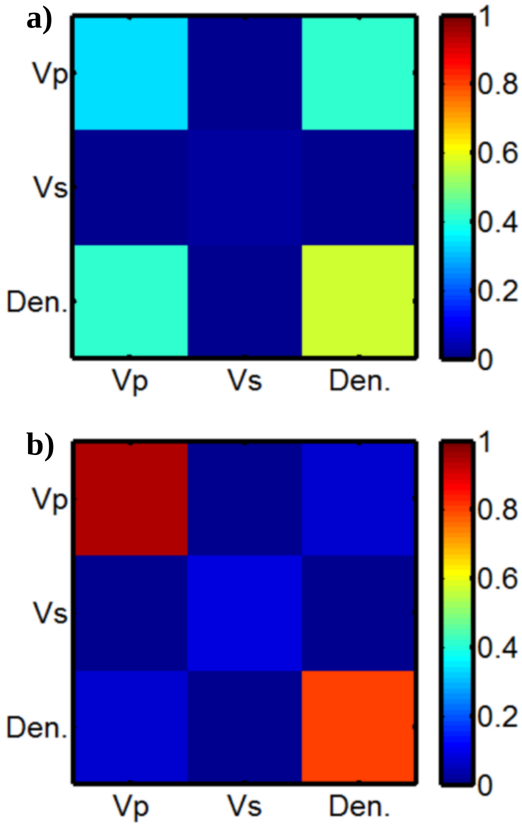

Figure 8: Model resolution matrices computed for the 0-30 and 0-60 degree inversions (a and b, respectively).

7. Synthetic inversions

To better understand the ability of the linearized Gauss-Newton inversion to determine the elastic properties of seabed sediments and to demonstrate the benefits of wide-angle reflections in constraining the inversion results, we perform synthetic inversions based on an analytical AVA response. The inversions are performed with two ranges of angles: 0-30 and 0-60 degrees.

The observed AVA response is computed using the Zoeppritz equations and considering the reference elastic model that was introduced previously. In the inversion, the water properties are fixed at the true values, and only the elastic properties of the seabed are considered as unknowns.

As is widely known, gradient-based methods are prone to becoming trapped in local minima if the initial model is not sufficiently accurate. To address this problem, the low computational effort of the forward modelling in linearized AVA inversion (i.e., the Zoeppritz equations) makes it feasible to perform different inversion runs that start from different initial models, which are randomly generated with uniform distributions over user-defined ranges of *Vp*, *Vs* and density. The final results will be the solution that minimizes the L_2 norm between the observed and predicted data for the considered range of angles (0-30 degrees or 0-60 degrees). Note that the non-linearity of the inversion increases as the range of angles increases. This demonstrates that the importance of a good initial model increases as the range of angles increases.

Let us consider the narrow-angle AVA inversion. Figure 9a shows the columns of the Jacobian matrix computed in the last iteration that pertain to the inversion run that results in the best data prediction. The first and last columns of this matrix (which correspond to *Vp* and density) play a major role in determining the R_{pp} response, whereas the *Vs* column has very small values that indicate its minor influence on the R_{pp} trend. Analysing the columns of the Jacobian matrix shows that the influence of *Vp* increases as the angle of incidence increases, whereas the influence of the density appears to remain nearly constant, at least within this limited range of angles, as the source-to-receiver distance increases (similar conclusions were drawn from Figures 1 and 2). Figure 9 also shows the convergence of the *Vp*, *Vs* and density estimates as a function of the iteration number. These figures show the rapid variations at the first iteration that characterized the predicted *Vp* and density values, whereas the variations in the predicted *Vs* with the iteration number are much smaller. As previously discussed, this is related to the negligible influence of *Vs* on the P-wave reflection coefficients. Figures 9b and 9d also clearly illustrate the cross-talk between the *Vp* and density terms that produces an overestimation of *Vp* and a consequent underestimation of the density. Obviously, the acoustic impedance that is obtained by multiplying these two parameters will be correctly estimated.

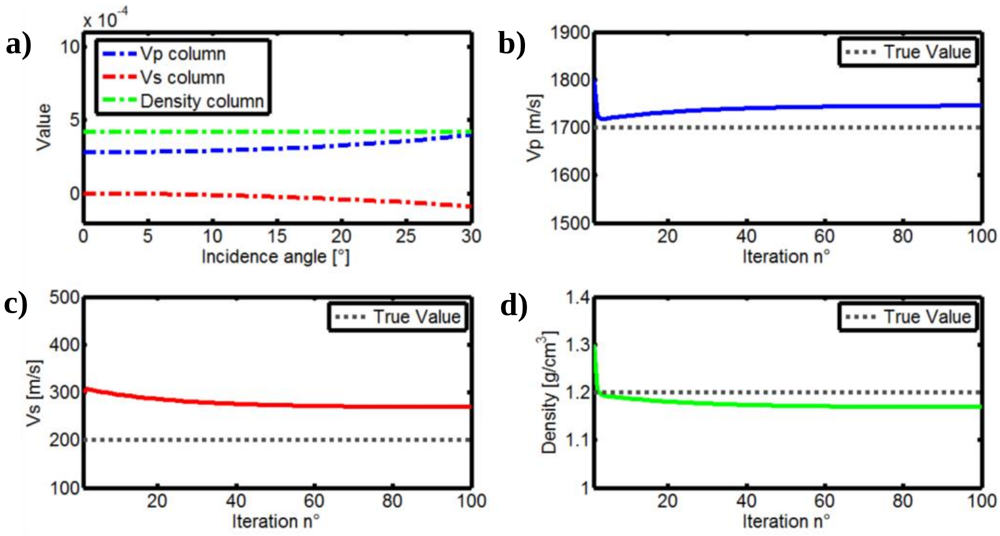

Figure 9: Results of the narrow-angle AVA inversion. a) The three columns of the Jacobian matrix. b), c) and d) The predicted seabed elastic properties as a function of the iteration number. Vp, Vs and density are shown in b), c), and d), respectively). In b), c) and d), the grey dotted lines indicate the true property values.

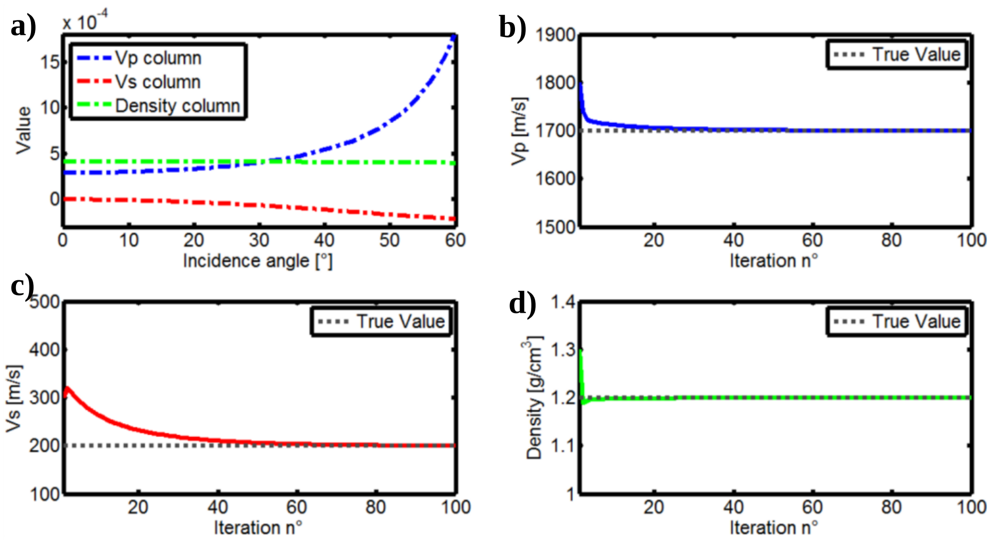

Figure 10: Results of the wide-angle AVA inversion. a) The three columns of the Jacobian matrix. b), c) and d) The predicted seabed elastic properties as a function of the iteration number. Vp, Vs and density are shown in b), c), and d), respectively). In b), c) and d), the grey dotted lines indicate the true property values.

Figure 10 shows the columns of the Jacobian matrix at the convergence point and the evolution of the estimated elastic properties for the wide-angle inversion. The influence of *Vp* becomes increasingly significant as the incidence angle increases, whereas the influences of *Vs* and density show minor variations compared to *Vp*. In particular, the increasing absolute values of the terms of the Jacobian matrix that pertain to *Vs* demonstrate that the influence of *Vs* increases as the incidence angle increases. Figures 10b and 10d show the rapid convergence of the *Vp* and density estimates toward the true values. A comparison of Figures 10b and 10c with the corresponding parts of Figure 9 shows that in the wide-angle inversion, we attain perfect estimations of *Vp* and density. In this wide-angle inversion, the *Vs* estimates converge toward the true value, although more slowly than the *Vp* and density estimates. These characteristics can be ascribed to the influence of the wide-angle reflections, which decreases the cross-talk between the inverted parameters and slightly increases the role of *Vs* in determining the P-wave reflection coefficients.

Figure 11 shows the marginal posterior probability density distributions for each seabed elastic parameter estimated by the Monte Carlo method while assuming Gaussian-distributed properties. Figure 11a and 11b show the marginal distributions for the narrow- and wide-angle AVA inversions, respectively. The results clearly indicate the greater resolution of *Vp* and density and the high uncertainties that affect the predicted *Vs* values. A comparison of Figures 11a and 11b shows that the uncertainties in the *Vp* and density estimations decrease significantly from the narrow-angle inversion to the wide-angle inversion, whereas the uncertainties in the *Vs* estimates decrease only slightly. These facts confirm the theoretical observations that were made in the previous sections and clearly demonstrate that in the case of very low *Vs* values, the wide-angle reflections become crucial for better constraining the *Vp* and density estimates, but they are not sufficient to significantly decrease the *Vs* uncertainty.

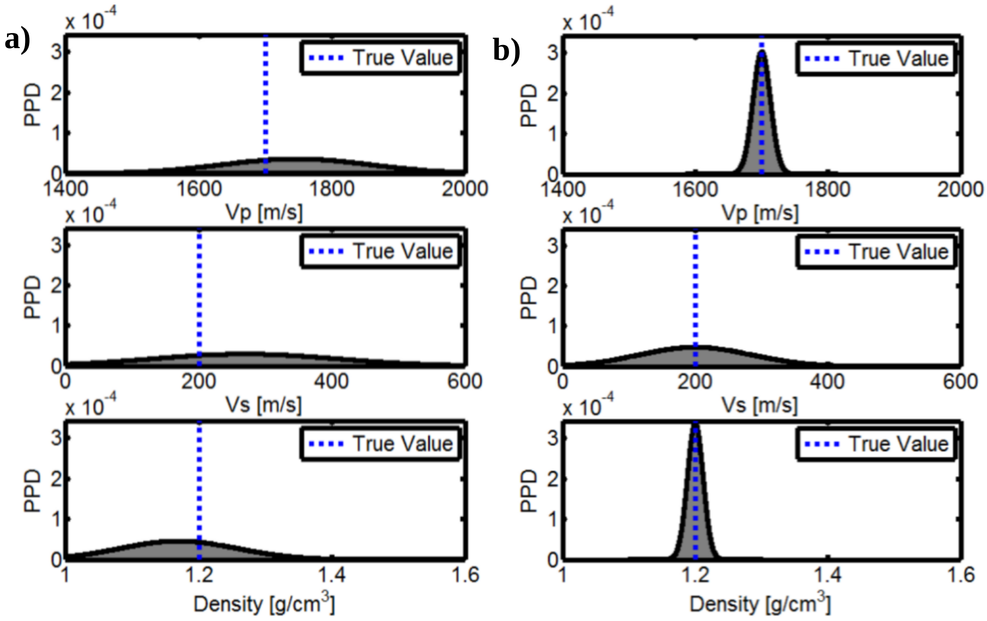

Figure 11: Predicted posterior marginal probability distributions for the Vp, Vs and density estimates in the synthetic inversion. a) and b) Show the narrow- and wide-angle inversions, respectively. For each case, Vp, Vs and density are shown from top to bottom, and the blue dotted lines indicate the true property values. To better compare the uncertainties associated with each elastic parameter the x- and y-axes are shown with the same scale.

Note that we have limited our attention to synthetic noise-free data. Random noise contamination would lead to similar results to the noise-free case in terms of the mean estimated properties; the only noteworthy difference would be the widths of the posterior distributions, which increase as the signal-to-noise ratio in the observed data decreases. We address the noise issue in the inversion of the field data in the next section.

8. Field data processing

The field data that are considered in this study are from a 2D well site survey (WSS) seismic line that was acquired offshore in the Adriatic Sea. The investigated area is characterized by a shallow and nearly flat sea bottom. Table 1 shows the most important recording and acquisition parameters.

Recording and Acquisition parameters	
Source Depth: 3 m	*Streamer Depth: 3 m*
Shot Interval: 12.5 m	*Group Interval: 12.5 m*
Number of Shots: 218	*Minimum Offset: 20 m*
Streamer Length: 600 m	*Record Lenght: 2048 ms*
Number of Groups: 48	*Sample Rate: 1 ms*

Table 1: Recording and acquisition parameters

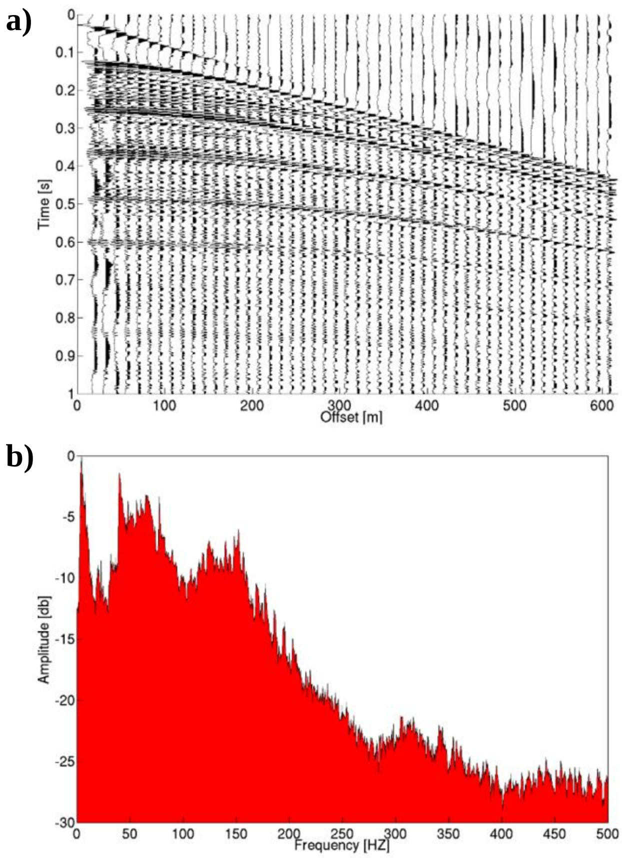

Figure 12: a) Example of raw shot gather and b) the related average amplitude spectrum.

Figure 12 shows an example of a raw shot gather and the corresponding average amplitude spectrum. The bandwidth of the spectrum ranges from 20 Hz to greater than 150 Hz, and the sampling rate was 1 ms, which resulted in a Nyquist frequency of 500 Hz. Low frequency noise can be recognized in both the time domain and the frequency domain near 5 Hz. The broadband recording coupled with the fine sampling rate in both time and space allows us to describe the subsurface features with a high degree of accuracy.

Taking into account the aim of this study, we process the data while paying particular attention to preserving and/or recovering the true amplitudes of the signals (Mazzotti and Ravagnan, 1995) and preserving the frequency content of the data. Therefore, no operator that could potentially alter the amplitude information or introduce artefacts is applied. Table 2 shows the flowchart of the processing sequence. We adopt a conservative processing sequence that does not use any multichannel operator, such as FX deconvolution, tau-P filter or any kind of amplitude boost that could potentially alter the physical meaning of the reflected signals. A pre-stack predictive deconvolution is applied in the common-offset domain to attenuate the sea bed multiples, and the estimated velocity model is used to convert the CDP gathers into the angle gathers that are necessary to perform the AVA inversion.

Processing sequence
1) Bandpass Filter
2) Trace editing and muting
3) Designature
4) Geometry Assignment
5) Velocity Analysis
6) Geometrical Spreading Correction
7) Predictive Deconvolution
8) Angle Gather Computation for AVA inversion
9) NMO correction and Stack
10) Kirchhoff Post-Stack Time Migration

Table 2: Flow-chart of the processing sequence.

Figure 13 shows the final time-migrated section up to 1 s. The section shows a simple geological setting with a flat seabed interface at approximately 120 ms and horizontal layers up to 500 ms that dip gently below 600 ms. The preserved high frequency content of the data is confirmed by the high resolution of the stack section. Figure 14 shows a close-up of the shallowest part of the subsurface beneath the seabed between CDP 100 and CDP 150 and down to 500 ms.

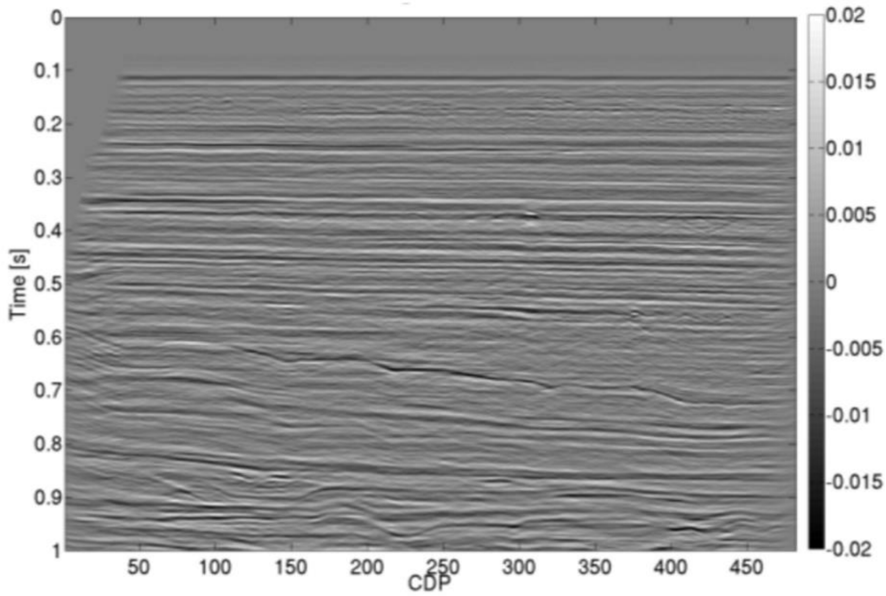

Figure 13: Stack section at the end of the processing sequence shown in Table 2.

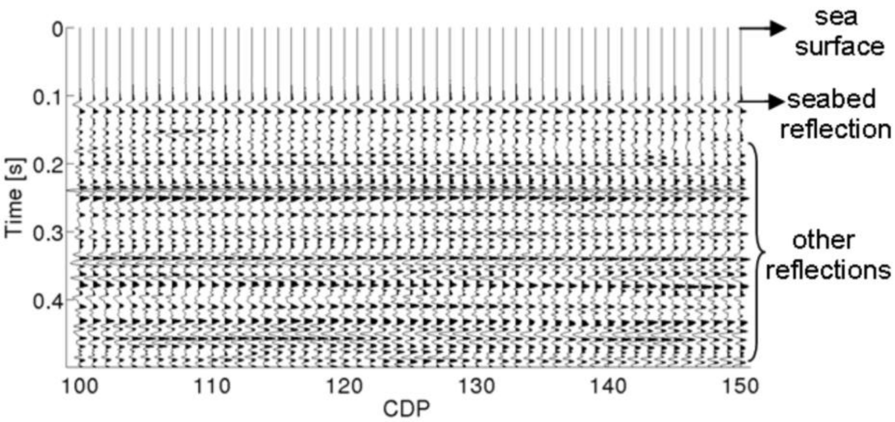

Figure 14: A close-up of Figure 13 highlighting the seabed and the shallowest part of the subsurface. The sea bottom and other primary reflections are indicated.

9. AVA inversion of field data

The limited water depth, the maximum offset, the high frequency content of the WSS data and the accurate processing sequence make it possible to extract the P-wave reflection coefficients with good reliability up to an incidence angle of 55-60 degrees. This allows us to compare the results of the narrow and wide-angle AVA inversions. The inversion was performed for each CDP with full fold along the 2D seismic line and considering two different ranges of angles: 0-30 and 0-60 degrees. In addition, limiting our attention to pre-critical reflections allows us to ignore the viscoelastic effects on the P-wave reflection coefficients, whereas the high frequency content of the data allows us to neglect the effects of a spherical wave front on the reflection coefficients. As in the synthetic inversion, the water properties are considered to be known and are fixed at 1500 m/s and 1 g/cm^3 for *Vp* and density, respectively.

Because we expect a class I AVA for the seabed reflection (Castagna and Swann, 1997), the AVA responses were extracted considering the peak amplitude of the seabed reflection. This AVA response was then properly re-scaled with respect to the peak amplitude of the seismic wavelet to derive the P-wave reflection coefficients. Figure 15 shows examples of seabed reflections and the associated P-wave reflection coefficients for a range of angles from 0 to 60 degrees. Note the increases of the reflection coefficient for incidence angles greater than 50 degrees as the critical angle is approached and the increase in scattering that affects the reflection coefficients as the incidence angle increases. This scattering can be ascribed to the interference between the seabed reflection and other reflected events.

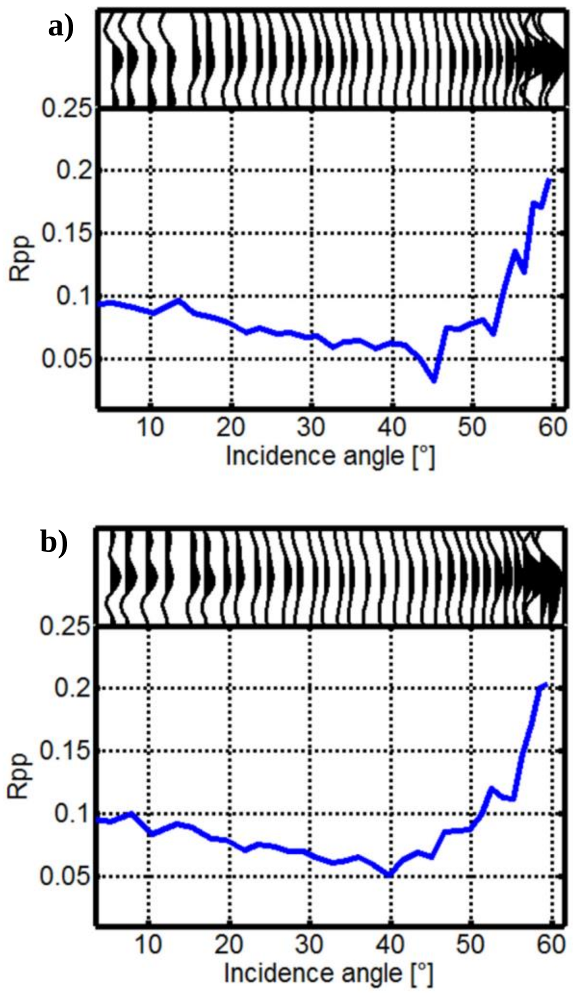

Figure 15: a) and b) Seabed-related reflections (top) and the associated R_{pp} responses (bottom) for two different CDPs along the seismic line.

As in the synthetic examples, to prevent the inversion from becoming stuck in local minima, the inversion is repeated several times starting from different initial guesses of the true model that were randomly generated with uniform distributions over user-defined ranges of *Vp*, *Vs* and density. The final solution for each CDP gather is the model that minimizes the L_2 norm between the observed and predicted P-wave reflection coefficients over the considered range of angles.

As previously discussed, the inversion process was stabilized with the Tikhonov approach, in which the damping parameter λ was chosen based on the trade-off curve. Figure 16 shows an example trade-off curve for one CDP gather and for the narrow-angle AVA inversion. An optimal choice for the λ parameter is between 0.1 and 0.01 because these values minimize both norms in the data space and model space.

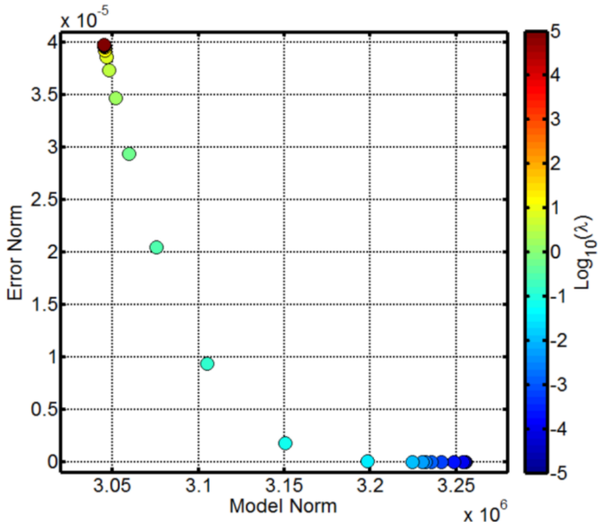

Figure 16: Example trade-off curve computed for a single CDP gather. A value of the regularization term λ between 0.1 and 0.01 allows us to minimize both norms in the data space (along the y-axis) and the model space (along the x-axis).

Figure 17 shows examples of observed and predicted AVA curves that are associated with the seabed reflections and pertain to the narrow-angle (Figures 17a and 17b) and wide-angle (Figures 17c and 17d) inversions. Good matches between the predicted and observed curves can be observed. Figures 18a and 18b represent the seabed's elastic properties estimated along the seismic line by the narrow- and wide-angle AVA inversions, respectively. In both figures, the *Vp*, *Vs* and density estimates are represented together with the associated uncertainties (estimated through 1000 Monte Carlo simulations). Both inversions yield similar results along the seismic line, which correspond to mean values of 1600 m/s, 200 m/s and 1.1 g/cm^3 for *Vp*, *Vs* and density, respectively. These values are associated with strongly unconsolidated sediments (as is usually the case for the seabed interface). However, a comparison of Figures 18a and 18b shows that wide-angle reflections are crucial for decreasing the uncertainties associated with *Vp* and density estimates and for stabilizing the inversion results (note that the scatter in the estimated values decreases from the narrow-angle inversion to the wide-angle inversion). Conversely, these reflections are not sufficient to better constrain the *Vs* estimates. In fact, in both inversions, the *Vs* profile is more scattered than the *Vp* and density profiles, and only a minor decrease in the uncertainties is visible in Figure 18b compared to Figure 18a. This fact confirms the conclusions that were drawn from the theoretical analysis and the synthetic inversions and demonstrates the difficulty of making a reliable *Vs* estimation in the case of low *Vs* values and high *Vp/Vs* ratios.

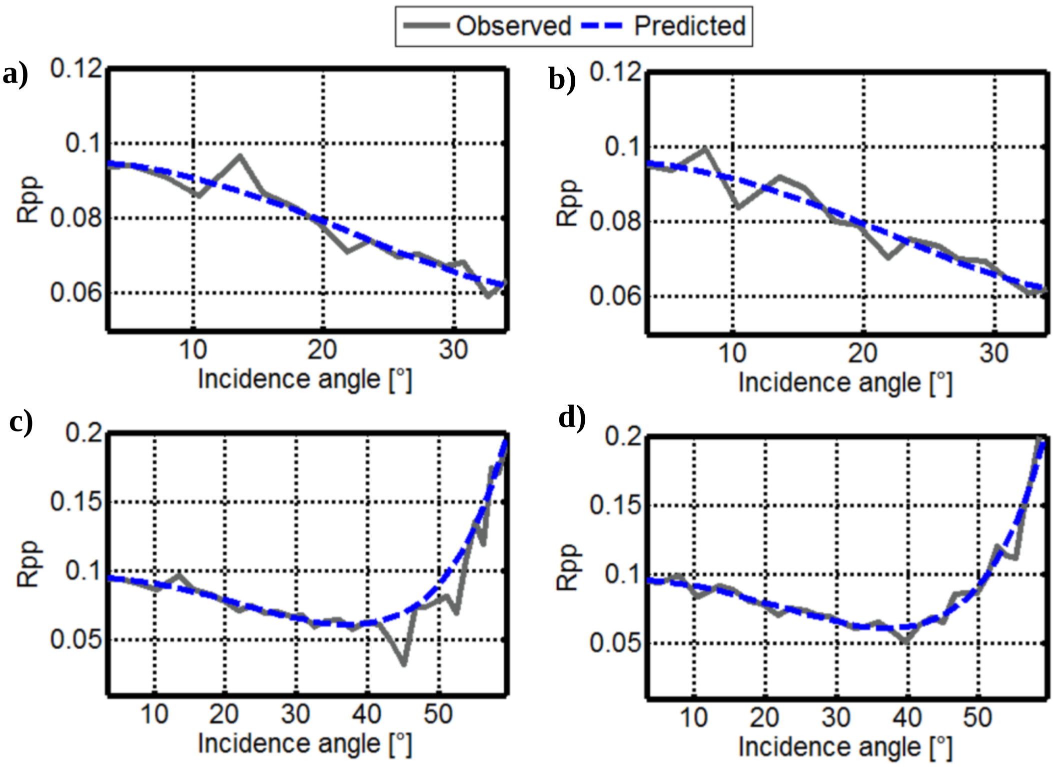

Figure 17: Examples of observed (continuous grey lines) and predicted (dotted blue lines) P-wave reflection coefficients for the seabed reflection extracted from 2 CDPs along the 2D seismic profile. a) and b) Correspond to the narrow-angle inversion, and c) and d) correspond to the wide-angle inversion.

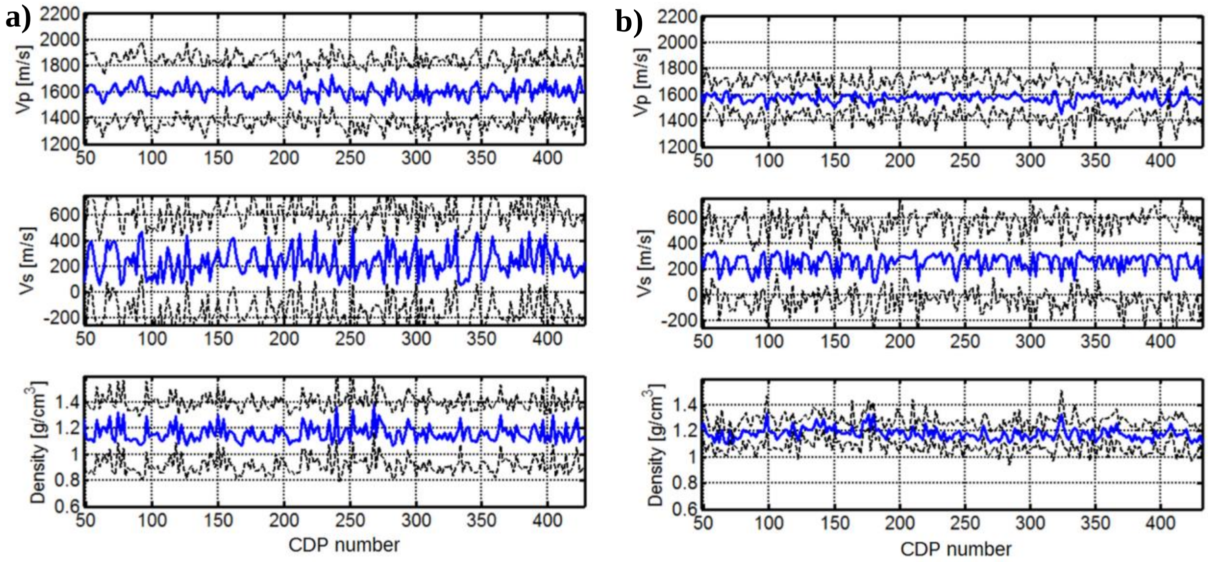

Figure 18: Elastic properties for the seabed interface estimated for each CDP position. a) and b) correspond to the narrow and wide-angle inversions, respectively. In both a) and b), Vp, Vs and density are shown from top to bottom. The blue lines indicate the mean estimated values, and the dotted black lines delimit the 95% confidence intervals. To better compare the uncertainty associated with each elastic parameter, the y-axes are shown with the same scale.

As previously discussed, Aleardi (2015) demonstrated that the cross-talk between the inverted parameters, and particularly for *Vp* and density, increases as the *Vp/Vs* ratio increases. This makes an independent estimation of the elastic parameters more problematic in the case of high *Vp/Vs* ratios. In addition, we have already determined that the cross-talk decreases as the range of angles considered in the inversion increases. In this field data inversion, to quantify the cross-talk between the inverted parameters and the role of wide-angle reflections in mitigating it, we compute the correlation matrices from the *Vp*, *Vs* and density profiles that were estimated by the two AVA inversions (Figure 19). A comparison of Figures 19a and 19b shows that the strong negative correlation (-0.91) between *Vp* and density and the positive correlations between *Vp* and *Vs* (0.5) that exist in the 0-30 degree inversion are considerably attenuated in the wide-angle inversion. This result is a practical demonstration that wide-angle reflections are essential for both increasing our confidence in the reliability of the final results and decreasing the cross-talk between the estimated elastic parameters.

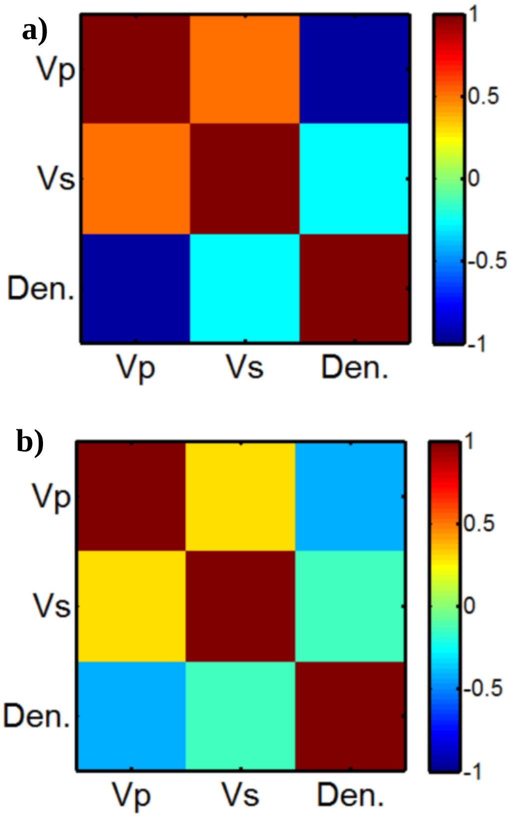

Figure 19: Correlation matrices for the narrow-angle and wide-angle AVA inversions (a and b, respectively) computed considering the results of the AVA inversions along the seismic line. Note the decrease in correlation among Vp and density and Vp and Vs when passing from the narrow- to the wide-angle inversion.

10 Conclusions

We applied a linearized AVA inversion to estimate the elastic properties of seabed sediments, and we analysed the influence of high *Vp/Vs* ratios on the inversion results and the benefits of wide-angle reflections in constraining the estimated properties. Using a simplified, single-interface seabed model and the Zoeppritz equations, we showed that in the case of high *Vp/Vs* ratios, the *Vs* contrast at the reflecting interface plays a very minor role in determining the P-wave reflection coefficients. We also demonstrated that the influence of the viscoelastic parameters can be neglected if the AVA inversion is limited to pre-critical incidence angles. The analysis of the error function of the AVA inversion and the application of the sensitivity analysis tools to the inversion kernel clearly demonstrated that in the case of high *Vp/Vs* ratios, wide-angle reflections are essential to decreasing both the cross-talk between the inverted parameters and the uncertainties in the *Vp*, *Vs* and density estimations. However, even using wide-angle reflections, *Vs* is the most poorly constrained parameter.

The application of linearized narrow- and wide-angle AVA inversions to both synthetic and WSS field data confirmed the conclusions that were drawn from the theoretical analysis. In particular, the application of narrow-angle inversion in the case of high *Vp*/*Vs* ratios yields final results that are characterized by a low reliability (high variance) of *Vs* estimates and a strong correlation (strong cross-talk) between *Vp* and density. While the inclusion of wide-angle reflections is crucial to decreasing the uncertainties associated with *Vp* and density estimates and mitigating the cross-talk between the inverted parameters, it is not sufficient to significantly decrease the uncertainties associated with *Vs*.

These peculiarities must be taken into account when classical angle-limited AVA inversion is applied to the investigation of underconsolidated or overpressured sediments, which are usually characterized by very low *Vs* values and very high *Vp/Vs* ratios. In addition, the S-wave velocity is a key parameter for a complete elastic description of the seabed interface. Therefore, in cases of high *Vp/Vs* ratios, more sophisticated approaches are likely needed to attain a more reliable elastic characterization of the seabed properties. One of these approaches could be pre-stack waveform inversion, which overcomes the limits of AVA inversion (e.g., single reflecting interface and no interferences between primaries and multiples) by exploiting the full information content of the data (kinematic, amplitude and phase information) and as many wave phenomena as possible (primaries, multiples, converted waves) to derive high-resolution quantitative models of the subsurface (Aleardi et al., 2015).

Appendix A. Sensitivity analysis in the case of a *Vp/Vs* ratio of 2

For a better understanding of the drawbacks that are introduced in the AVA inversion by high *Vp/Vs* ratios, we briefly comment on the results of the sensitivity analysis of the Jacobian matrix that is derived for the case of a *Vp/Vs* ratio of 2, which is often assumed in deep hydrocarbon exploration. The Jacobian matrix that is used in the following sensitivity analysis is derived from the inversion of a simplified model composed of two homogeneous and elastic half-spaces with a background *Vp/Vs* ratio of two. In the inversion, the elastic properties of the upper layer are fixed at their true values, and only the properties of the lower layer are considered as unknowns. We refer the reader to Aleardi (2015) for a more detailed analysis of linear AVA inversions in the case of high *Vp/Vs* ratios.

We start by describing the eigenvector in the model space that is derived from the SVD decomposition of the Jacobian matrix (see section 6). In Figure A1, we note that, as expected, the first eigenvector points toward the P-impedance for low incidence angles. However, for incidence angles greater than 25 degrees, the density component decreases, and the *Vs* component increases significantly. The second eigenvector points toward the *Vs* parameter for low incidence angles and toward the density parameter for high incidence angles. The influence of *Vp* on this second eigenvector is negligible for the range of angles that we consider. The physical meaning of the third eigenvector is more difficult to interpret because it depends on different combinations of all three parameters. However, if we consider a limited range of angles (up to 25-30 degrees), the *Vs* parameter can be reliably estimated from the second eigenvector, whereas the independent estimation of *Vp* and density is more problematic, and only the P-impedance values can be reliably derived. If we consider a wider range of angles (up to 50-60 degrees), *Vs* can be estimated from both the first and second eigenvectors, and *Vp* and density can be independently estimated from the first and second eigenvectors. In particular, the information contained in the second eigenvector for incidence angles greater than 45 degrees can be used to make independent estimations of *Vp* and density. The differences between the

Vp/Vs=2 and the *Vp/Vs>2* cases clearly stand out when Figure 7 and Figure A1 are compared. In particular, in Figure 7, note the null influence of the *Vs* parameter in the first eigenvector and the higher cross-talk between *Vp* and density in both the first and second eigenvectors.

Finally, we describe the model resolution matrices that are computed with a *Vp/Vs* ratio of 2 and for two ranges of incidence angles: 0-30 and 0-60 degrees (Figures A2a and A2b, respectively). In the case of a range of angles of 0-30 degrees, we observe good resolutions for *Vp* and density and a slightly lower resolution for *Vs*. The off-diagonal terms indicate the strong cross-talk between *Vp* and density and between *Vs* and density. Extending the range of angles to 60 degrees (Figure A2b) results in perfect resolutions for all three parameters and produces strong attenuations of the *Vp*-density and the *Vs*-density cross-talks. The comparison between Figure A2 and Figure 8 demonstrates the increase in the *Vs* resolution and the decrease in cross-talk for a *Vp/Vs* ratio of two.

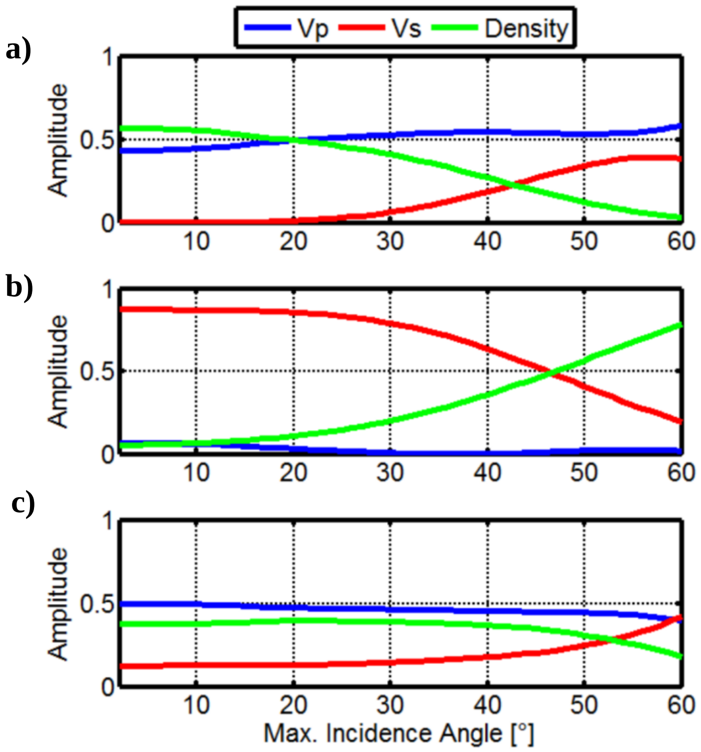

Figure A1: Eigenvectors in the model space versus the maximum observation angle for a Vp/Vs ratio of 2. The components of the first, second and third eigenvectors are represented in a), b) and c), respectively.

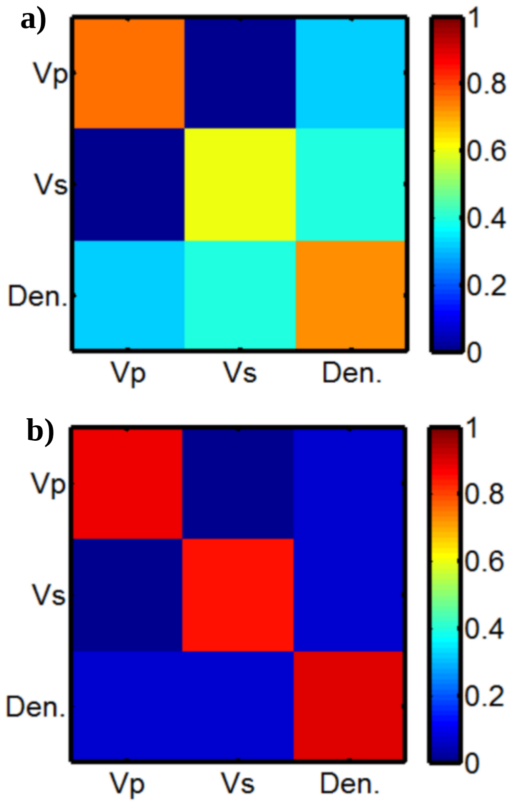

Figure A2: Model resolution matrices computed for the 0-30 and 0-60 degree inversions and considering a Vp/Vs ratio of 2 (a and b, respectively).

References

Aki, K., and Richards, P.G. (1980). Quantitative seismology: Theory and methods. WH Freeman and Co.

Aleardi M. (2014). Seismic inversion methods for overpressure prediction and elastic seabed characterization. PhD Thesis. University of Pisa.

Aleardi, M. (2015). The importance of the Vp/Vs ratio in determining the error propagation, the stability and the resolution of linear AVA inversion: a theoretical demonstration. Bollettino di Geofisica Teorica e Applicata, 56(3), 357-366.

Aleardi, M., Tognarelli, A., and Mazzotti, A. (2015). Characterization of Shallow Marine Sediments by Means of High Resolution Velocity Analysis and Stochastic 1D FWI. In proceedings of Near Surface Geoscience 2015-21st European Meeting of Environmental and Engineering Geophysics. Doi: 10.3997/2214-4609.201413804.

Alulaiw, B., and Gurevich, B. (2013). Analytical wavefront curvature correction to plane-wave reflection coefficients for a weak-contrast interface. Geophysical Prospecting, 61(1), 53-62.

Amundsen, L., and Reitan, A. (1995). Estimation of sea-floor wave velocities and density from pressure and particle velocity by AVO analysis. Geophysics, 60(5), 1575-1578.

Aster, R. C., Borchers, B., and Thurber, C.H. (2005). Parameter estimation and inverse problems. Elsevier Academic Press.

Avseth, P., Mukerji, T., and Mavko, G. (2005). Quantitative seismic interpretation: Applying rock physics tools to reduce interpretation risk. Cambridge university press.

Ayres, A., and Theilen, F. (1999). Relationship between P- and S-wave velocities and geological properties of near-surface sediments of the continental slope of the Barents Sea. Geophysical Prospecting, 47, 431-441.

Castagna, J. P., and Swan, H. W. (1997). Principles of AVO crossplotting. The leading edge, 16(4), 337-344.

Downton, J. E. (2005). Seismic parameter estimation from AVO inversion: Ph.D. dissertation, University of Calgary.

Drufuca G., and Mazzotti, A. (1995). Ambiguities in AVO inversion of reflections from a gas-sand. Geophysics, 60(1), 134-141.

Grana, D., and Della Rossa, E. (2010). Probabilistic petrophysical-properties estimation integrating statistical rock physics with seismic inversion. Geophysics, 75(3), O21-O37.

Grion S., Mazzotti A., and Spagnolini, U. (1998). Joint estimation of AVO and kinematic parameters. Geophysical Prospecting, 46, 405-422.

Hamilton, E. L., (1976). Variations of density and porosity with depth in deepsea sediments. Journal of Sedimentary Petrology, 46, 280–300.

Jensen, F. B., Kuperman, W. A., Porter, M. B., and Schmidt, H. (2011). Computational ocean acoustics. Springer.

Mazzotti, A. (1990). Prestack amplitude analysis methodology and application to seismic bright spots in the Po Valley, Italy. Geophysics, 55(2), 157-166.

Mazzotti, A., and Ravagnan, G. (1995). Impact of processing on the amplitude versus offset response of a marine seismic data set. Geophysical prospecting, 43(3), 263-281.

Mazzotti, A., and Zamboni, E. (2003). Petrophysical inversion of AVA data. Geophysical Prospecting, 51(6), 517-530.

Ostrander, W. (1984). Plane-wave reflection coefficients for gas sands at non-normal angles of incidence. Geophysics, 49(10), 1637-1648.

Riedel, M., and Theilen, F. (2001). AVO investigations of shallow marine sediments. Geophysical Prospecting, 49(2), 198-212.

Riedel, M., Dosso, S. E., and Beran, L. (2003). Uncertainty estimation for amplitude variation with offset (AVO) inversion. Geophysics, 68(5), 1485-1496.

Rutherford, S.R., and Williams, R.H. (1989). Amplitude-versus-offset variations in gas sands. Geophysics, 54(6), 680-688.

Skopintseva, L., Ayzenberg, M., Landrø, M., Nefedkina, T., and Aizenberg, A. M. (2011). Long-offset AVO inversion of PP reflections from plane interfaces using effective reflection coefficients. Geophysics, 76(6), C65-C79.

Skopintseva, L., and Alkhalifah, T. (2013). An analysis of AVO inversion for postcritical offsets in HTI media. Geophysics, 78(3), N11-N20.

Tarantola, A. (2005). Inverse problem theory and methods for model parameter estimation. Siam.

Theilen, F., and Pecher, I.A. (1990). Assessment of shear strength of the sea bottom from shear wave velocity measurements on box cores and in-situ. In: Shear Waves in Marine Sediments (eds J.M. Hovem et al.). Kluwer Academic Publishers.

Ursenbach, C. P., Haase, A. B., and Downton, J. E. (2007). An efficient method for avo modeling of reflected spherical waves. Journal of Seismic Exploration,16(1), 79-104.

Wang, Y. (2003). Seismic amplitude inversion in reflection tomography. Elsevier.

Zhu, X., and McMechan, G.A. (2012). Elastic inversion of near-and postcritical reflections using phase variation with angle. Geophysics, 77(4), R149-R159.

Zoeppritz, K. (1919). On the reflection and propagation of seismic waves at discontinuities. Erdbebenwellen, VIIB, 66-84.